AN EFFICIENT AND MIXED HETEROGENEOUS MODEL FOR IMAGE RESTORATION

Yubin Gu^{1,*}, Yuan Meng^{1,*}, Kaihang Zheng^{1,*}, Xiaoshuai Sun^{1,†} Jiayi Ji^{1,2}, Weijian Ruan³, Liujuan Cao¹, Rongrong Ji¹

¹MAC Lab, Xiamen University, China
 ²National University of Singapore, Singapore
 ³Smart City Research Institute, China Electronics Technology Group Corporation, China

April 16, 2025

ABSTRACT

Image restoration (IR), as a fundamental multimedia data processing task, has a significant impact on downstream visual applications. In recent years, researchers have focused on developing generalpurpose IR models capable of handling diverse degradation types, thereby reducing the cost and complexity of model development. Current mainstream approaches are based on three architectural paradigms: CNNs, Transformers, and Mambas. CNNs excel in efficient inference, whereas Transformers and Mamba excel at capturing long-range dependencies and modeling global contexts. While each architecture has demonstrated success in specialized, single-task settings, limited efforts have been made to effectively integrate heterogeneous architectures to jointly address diverse IR challenges. To bridge this gap, we propose RestorMixer, an efficient and general-purpose IR model based on mixed-architecture fusion. RestorMixer adopts a three-stage encoder-decoder structure, where each stage is tailored to the resolution and feature characteristics of the input. In the initial high-resolution stage, CNN-based blocks are employed to rapidly extract shallow local features. In the subsequent stages, we integrate a refined multi-directional scanning Mamba module with a multi-scale window-based self-attention mechanism. This hierarchical and adaptive design enables the model to leverage the strengths of CNNs in local feature extraction, Mamba in global context modeling, and attention mechanisms in dynamic feature refinement. Extensive experimental results demonstrate that RestorMixer achieves leading performance across multiple IR tasks while maintaining high inference efficiency. The official code can be accessed at https://github.com/ClimBin/RestorMixer.

1 Introduction

Image restoration (IR) is a fundamental task in multimedia visual data processing, aimed at recovering high-quality, clear images from degraded or damaged images. As a critical pre-processing step, IR significantly affects the performance of downstream visual applications, such as object detection [1], image segmentation [2], and video analysis [3]. Therefore, IR has become an integral component of modern visual system data processing pipelines.

Traditionally, IR models have been designed for specific tasks, such as deraining [4, 5], desnowing [6, 7], and super-resolution (SR) [8, 9]. While these task-specific models typically achieve excellent performance, they are costly in terms of development and deployment. Each task requires specialized architecture design and corresponding model settings, which lowers efficiency in both research and practical applications. With the rapid development of deep learning technologies, there has been increasing interest in developing general-purpose IR models capable of handling multiple types of degradation within the same types of frameworks. These models have shown a tendency to either approach or even surpass the performance of task-specific expert models. Such models not only reduce design and

^{*}Equal contribution.

[†]Corresponding author.

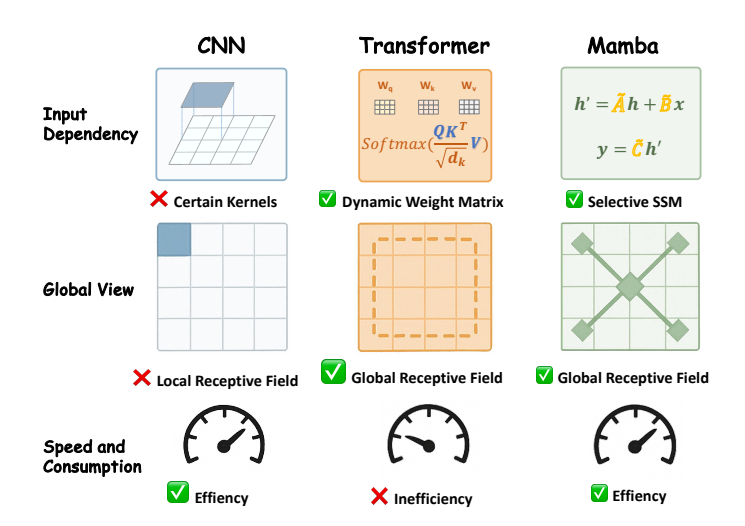


Figure 1: Comparison of three mainstream architectures in terms of input dependency, global view, and inference speed.

deployment costs but also promote scalability and adaptability across diverse IR tasks. Thus, general-purpose IR models represent a meaningful and promising research direction, as they can significantly lower development costs while achieving performance comparable to expert models.

Recent works have proposed general-purpose IR models, primarily focusing on three major architectures: Convolutional Neural Networks (CNN), Transformers, and Mamba-based architecture. Fig. 1 shows the advantages of different design mechanisms. For instance, the CNN-based IRNeXt [10] leverages the efficiency and locality of convolutions to effectively extract shallow features. Restormer [11] and SwinIR [12] are Transformer-based models that utilize various self-attention mechanisms to model global feature long-range dependencies and window-granularity feature relationships, enhancing the model's dynamic perception of features. These models outperform earlier CNN-based models, though at the cost of slower inference speed. Additionally, the recently proposed Mamba [13] model incorporates unique hardware-aware and parallel scanning mechanisms that accelerate global modeling, offering a new foundational structure for IR models. For example, VmambaIR [14] and MambaIR [15] introduce innovative scanning mechanisms to establish global dependencies of visual features in multiple directions, addressing limitations of the vanilla Mamba in handling visual data with non-causal relationships. However, they overlook issues of feature redundancy and computational deficiency caused by multi-directional scanning and memory loss due to long sequences. These methods offer diverse perspectives on general-purpose IR design, focusing on single-structure-based solutions, yet they overlook the potential benefits of integrating heterogeneous designs to address the diversified challenges of IR tasks. Consequently, existing general-purpose IR models often exhibit suboptimal performance due to the inability to fully exploit the complementary advantages of different architectural designs.

To address the research gap in heterogeneous architecture design for general-purpose IR models, we propose RestorMixer - a novel hierarchical framework integrating complementary architectural paradigms. The model employs a three-stage encoder-decoder architecture with progressive downsampling/upsampling operations for multi-scale feature learning. Each stage is specifically optimized according to inherent scale characteristics: In the high-resolution initial stage, lightweight convolutional blocks efficiently extract shallow features through local receptive fields, prioritizing fine-grained detail preservation with minimal inference overhead. Subsequent stages implement a mixed architecture M-T blocks combining: 1) Enhanced Memory Visual Mamba (EMVM) blocks for global dependency modeling, and 2) Multi-scale Window-based Transformer blocks that dynamically refine multi-ranged local representations through attention-guided feature recalibration. This strategic integration synergizes CNN's local inductive bias, Mamba's linear-complexity global modeling, and Transformer's adaptive feature optimization. Experimental validation demonstrates that RestorMixer achieves leading performance on both single/mixed degradation benchmarks while maintaining superior inference efficiency, as shown in Fig. 2. In general, our contributions can be summarized as follows:

• We analyze the limitations of existing general-purpose IR models that focus on single-architecture design paradigms and emphasize the necessity of adopting a mixed structure fusion approach to address the diverse requirements of IR.

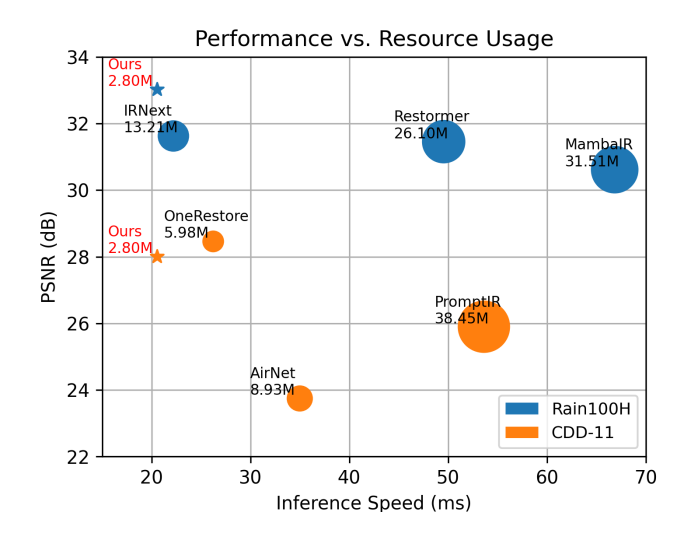


Figure 2: Comparison of RestorMixer with various representative methods in terms of performance, inference speed, and number of parameters. Testing is at the same input size.

- We propose RestorMixer, a multi-stage encoder-decoder IR model that effectively integrates CNN, Mamba, and Transformer. This design not only leverages the strengths of each design but also optimizes their combination and collaboration based on the characteristics of features.
- Through extensive experiments on various benchmarks, including single-degradation and mixed-degradation datasets, we demonstrate that RestorMixer achieves leading performance while maintaining efficient inference.

2 Related Work

2.1 Image Restoration

Image Restoration (IR) seeks to recover high-quality images from degraded inputs. It is a central challenge in multimedia data processing due to its ill-posed nature and diverse subtasks. Over the past decade, research has shifted from traditional handcrafted feature extraction methods to data-driven deep neural network-based learning models, which have become mainstream due to their superior performance. Researchers have explored multiple subtasks, such as rain streak removal [4], super-resolution [8], and mixed degradation IR [16] et al. For example, Wang et al. [17] proposed a model for rain removal using local and non-local interactions and multi-scale deep learning. In super-resolution, SRCNN [9] pioneered the use of deep learning with a shallow convolutional neural network. Besides, Zhan et al.'s AnySR [8] further reconstructs arbitrary-scale super-resolution methods for flexible resource allocation. However, specialized models for specific degradations have limited generalizability. Recent research has focused on developing general IR models [10, 11, 12, 15, 18] to handle multiple tasks with a single architecture. Existing general-purpose IR models are based on single architectural frameworks like CNNs, Transformers, and state space models (e.g., Mamba). CNN-based methods like MPRNet [19] and IRNeXt [10] offer robust feature extraction for universal restoration. Transformer-based models like Restormer [11] and SwinIR [12] capture long-range dependencies but face computational complexity issues. Recently, state space models such as Mamba [13] have gained attention for their computation ability and long-sequence modeling capabilities. Although CNNs have distinct advantages in inference speed, Transformers in global modeling, and Mamba in efficient long-range modeling, few studies have explored the integration of these triple heterogeneous foundational architectures for general-purpose IR.

2.2 State Space Models

State space models (SSMs), originally inspired by classical control theory, have emerged as a novel backbone in deep learning, particularly excelling in modeling long-sequence data. By incorporating linear extrapolation properties, these models have achieved breakthrough progress in long-range dependency modeling, attracting significant research interest. Notably, Mamba [13], a new generation of input-dependent SSMs, has demonstrated Transformer-like performance in natural language processing (NLP), with computational complexity linear in input length, thanks to its selective mechanism and hardware-efficient ability. The success of Mamba has spurred its application in vision tasks, including image classification [20] and biomedical image segmentation [21]. Recent innovations [22, 20, 23, 14] based on

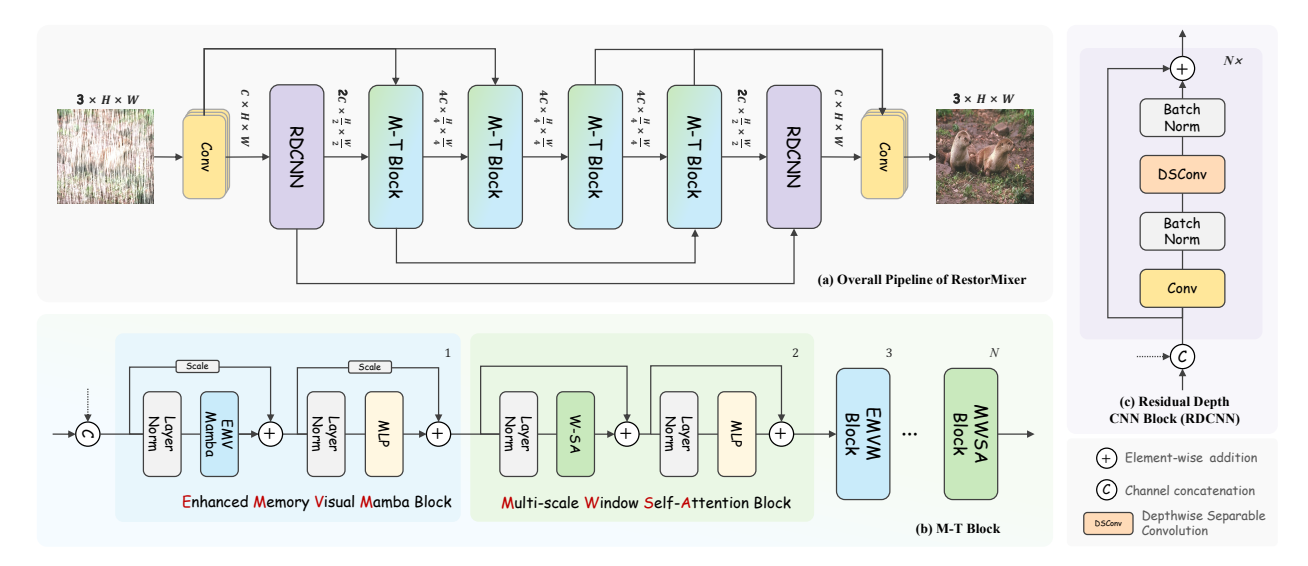


Figure 3: Framework of **RestorMixer**. (a) Overall pipeline. (b) Structure of the M-T Blocks, composed of alternating Enhanced Memory Visual Mamba Blocks (EMVM) and Multi-scale Window Self-Attention (MWSA) Blocks. (c) Residual Depth CNN Block (RDCNN), built with a stack of basic residual convolutional units.

Vision Mamba [24] have shown promise. In the IR domain, models such as MambaIR [15] and VMambaIR [14] have demonstrated significant potential. For example, MambaIR [15] combined visual SSMs with improved MLP to address local pixel forgetting and channel redundancy in traditional Mamba. However, Mamba's unidirectional scanning mechanism limits its performance in image data processing and in-context learning compared to Transformers. Although multi-directional scanning mechanisms have mitigated some of these limitations for non-causal image data, they introduce computational redundancy and insufficient local feature association. To address these challenges, this work introduces an optimized scanning mechanism in the encoder-decoder's latter two low-resolution feature processing stages, combining Mamba with a simple multi-scale window-based Transformer structure. This approach effectively resolves issues of computational redundancy and insufficient local feature association.

3 The Proposed Model: RestorMixer

3.1 Overview of Architecture

We introduce RestorMixer, a novel IR model that integrates heterogeneous structures. Fig. 3 (a) shows that RestorMixer differs from prior single-structure models (e.g., CNN, Transformer, Vision Mamba) by combining three foundational designs tailored to the feature properties processed at different encoder/decoder stages, ensuring synergistic interaction.

The model comprises two main blocks: the Residual Depth CNN Block (RDCNN) and the Mamba-Transformer Block (M-T), distinguished by colored blocks in Fig. 3 (a). Given a degraded input image $\mathcal{I}_{low} \in \mathbb{R}^{H \times W \times C}$, the model first adopts a CNN stem to expand input channels, yielding $\mathcal{I}'_{low} \in \mathbb{R}^{H \times W \times C}$ (with C=32 channels). The encoding process involves three stages, each handling features at different scales. Specifically, \mathcal{I}' passes through the Residual Depth CNN Block (RDCNN), as shown in Fig. 3 (c) to extract shallow features $\mathcal{I}_e^1 \in \mathbb{R}^{H \times W \times C}$, followed by a convolutional downsampling layer that halves the spatial scale and doubles the channels to produce $\mathcal{I}_e^2 \in \mathbb{R}^{\frac{H}{2} \times \frac{W}{2} \times 2C}$. \mathcal{I}_e^2 is then concatenated with the corresponding downsampled input features $\mathcal{I}'_{/2} \in \mathbb{R}^{\frac{H}{2} \times \frac{W}{2} \times C}$ and fed into the M-T Block (as shown in Fig. 3 (b)). This process continues to generate three multi-scale feature maps in the encoder. In the decoder, M-T Blocks process lower-resolution feature maps, while RDCNN block handles the highest-resolution features. Additionally, we employ a deep supervision strategy during optimization, enabling each decoder stage to produce predictions at corresponding scales for loss calculation against reference images. Next, we detail the three foundational blocks comprising RestorMixer.

3.2 The Heterogeneous Designed Modules

RestorMixer combines three main heterogeneous structures with a focus on enhancing module collaboration. For large feature maps in high-resolution spaces, a rational RDCNN block is used due to its efficiency in extracting shallow

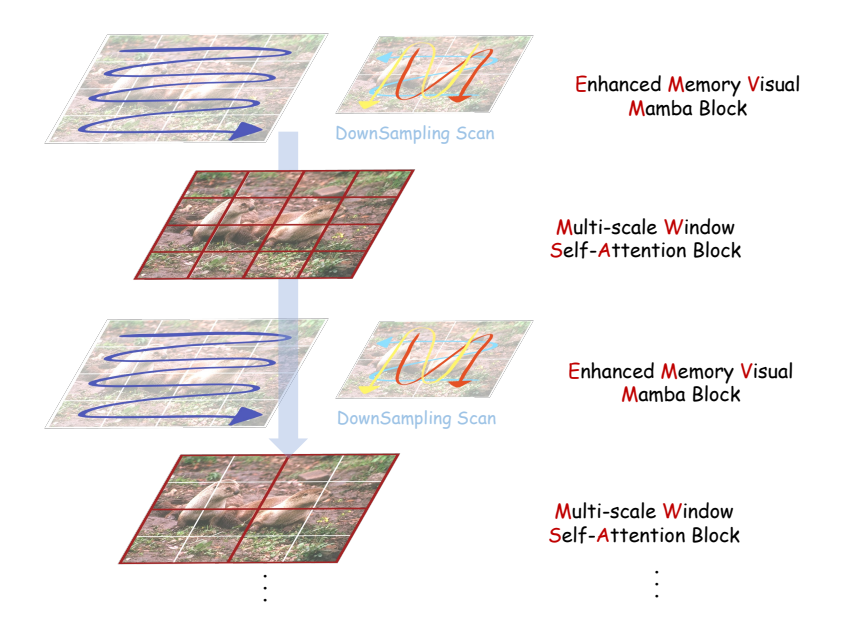


Figure 4: Illustration of the M-T Block. It is constructed by alternately stacking EMVM blocks with four-directional scanning and MWSA blocks to jointly capture long-range dependencies and local multi-scale features.

features and parallel processing capability. For two lower-resolution stages, modules based on Mamba and Transformer architectures are alternated to model long-range dependencies and refine local representations.

3.2.1 Residual Depth CNN Block

We designed the Residual Depth CNN Block (RDCNN) to process first-stage input features, which integrates standard convolution and depthwise separable convolution, as shown in Fig. 3 (c). For an input feature map $\mathbf{X} \in \mathbb{R}^{H \times W \times C}$, the spatial feature extraction is formulated as:

$$\mathbf{Y}_1 = \text{GELU}\left(\text{BN}\left(\text{Conv}_{3\times3}(\mathbf{X})\right)\right),\tag{1}$$

where BN(\cdot) and GELU(\cdot) are the Batch Normalization and the activation function, respectively. Standard 3×3 convolution captures fine-grained local textures and high-frequency patterns critical for IR, such as edge reconstruction and noise suppression. Subsequent processing employs a depthwise separable convolution to decouple spatial filtering and channel interaction:

$$\mathbf{Y}_{dw} = \text{Depth-Conv}_{3\times3}(\mathbf{Y}_1), \quad \mathbf{Y}_{pw} = \text{Point-Conv}_{1\times1}(\mathbf{Y}_{dw}),$$
 (2)

which reduce the computational complexity from $\mathcal{O}(C_{\text{in}}C_{\text{out}}K^2)$ to $\mathcal{O}(C_{\text{out}}(K^2+C_{\text{in}}))$. This design leverages the complementary strengths of both operations: the standard convolution preserves spatially correlated details essential for pixel-wise restoration, while the depthwise separable convolution minimizes redundant parameters, enhancing efficiency for large-scale feature maps of the first stage. The residual connection:

$$\mathbf{Y}_{\text{out}} = \text{GELU}\left(\text{BN}(\mathbf{Y}_{pw}) + \mathbf{X}\right),\tag{3}$$

ensures stable gradient flow and feature reuse, mitigating information loss in the IR model. This module is located at the beginning of the encoding stage and the end of the decoding stage to efficiently process the feature map of the largest scale, effectively extract and express shallow features, and both provide favorable conditions for the subsequent encoding stage and the final prediction output.

3.2.2 Enhanced Memory Visual Mamba

Initially, we provide a brief introduction to the State Space Models (SSM). SSMs map an input sequence $x(t) \in \mathbb{R}^L$ to a latent representation $h(t) \in \mathbb{R}^N$ and predict an output sequence $y(t) \in \mathbb{R}^L$. Mathematically, they are described by:

$$h'(t) = \mathcal{A}h(t) + \mathcal{B}x(t), \quad y(t) = \mathcal{C}h(t), \tag{4}$$

where $A \in \mathbb{R}^{N \times N}$, $B \in \mathbb{R}^{N \times 1}$, and $C \in \mathbb{R}^{1 \times N}$ are learnable parameters. To adapt SSMs for deep learning frameworks, discretization is applied using a timescale parameter $\Delta \in \mathbb{R}$ and the zero-order hold (ZOH) rule. The discretized equations become:

$$h(t) = \bar{\mathcal{A}}h(t-1) + \bar{\mathcal{B}}x(t), \quad y(t) = \mathcal{C}h(t), \tag{5}$$

where $\bar{\mathcal{A}}=e^{\Delta\mathcal{A}}$ and $\bar{\mathcal{B}}=(\Delta\mathcal{A})^{-1}(e^{\Delta\mathcal{A}}-I)\Delta\mathcal{B}\approx\Delta\mathcal{B}$, with I as the identity matrix. This process can be implemented as a global convolution:

$$y = x \odot \mathcal{K}, \quad \mathcal{K} = [\mathcal{CB}, \mathcal{CAB}, \dots, \mathcal{CA}^{L-1}\mathcal{B}],$$
 (6)

where $K \in \mathbb{R}^L$ is the convolution kernel. Furthermore, the Selective State Space mechanism equipped with the popular Mamba model enhances SSMs by making parameters \mathcal{B}, \mathcal{C} , and Δ input-dependent. Such a design enhances the model's input perception ability.

Recent IR methods have incorporated multi-directional scanning mechanisms to leverage Mamba's efficient sequence modeling capabilities and address the lack of multi-perspective modeling at the single-pixel level in vanilla Mamba. While this approach mitigates issues with uni-directional scanning in visual data processing, it introduces redundant computations and memory decay in single scans. To address these challenges, we propose the Enhanced Memory Visual Mamba (EMVM) module, as illustrated in Fig. 3 (b, blue block) and Fig. 4. EMVM adopts a multi-directional scanning strategy, processing visual sequences through horizontal forward (hf), horizontal backward (hb), vertical forward (vf), and vertical backward (vb) scans. Unlike previous methods [15, 14], EMVM optimizes for single-direction forgetting and reduces redundant computations across multiple directions, thereby enhancing model performance.

Specifically, given an $\mathbf{X} \in \mathbb{R}^{H \times W \times C}$, EMVM first performs Layer Normalization on the \mathbf{X} to obtain \mathbf{X}' :

$$\mathbf{X}' = \text{LayerNorm}(\mathbf{X}),\tag{7}$$

Then, \mathbf{X}' is reorganized in the horizontal forward direction to obtain $\mathbf{X}_{hf} \in \mathbb{R}^{HW \times C}$, followed by the selective state-space modeling to capture the transformation patterns for IR:

$$\mathbf{Y}_{\mathbf{hf}} = \mathbf{S}^{3}\mathbf{M}(\mathbf{X}_{\mathbf{hf}}) = \text{SelectiveSSM}\left(\text{Linear}(\mathbf{X}_{\mathbf{hf}})\right),$$
 (8)

where the state-space dynamics adapt to input content through discretized parameters $\bar{\mathcal{A}}, \bar{\mathcal{B}}$:

$$h_t = \bar{\mathcal{A}} \odot h_{t-1} + \bar{\mathcal{B}} \odot x_t'. \tag{9}$$

Besides, to reduce computational redundancy in multi-directional scanning and enhance scanning memory, we first downsample the input feature map \mathbf{X}' by a factor of 2. Then, we re-sequence the data according to specific directions to obtain $\mathbf{X}_{hb} \in \mathbb{R}^{\frac{H}{2} \times \frac{W}{2} \times C}$, $\mathbf{X}_{vf} \in \mathbb{R}^{\frac{H}{2} \times \frac{W}{2} \times C}$, and $\mathbf{X}_{vb} \in \mathbb{R}^{\frac{H}{2} \times \frac{W}{2} \times C}$. Each directional sequence is modeled similarly to \mathbf{X}'_{hc} :

$$\{\mathbf{X_{hb}}, \mathbf{X_{vf}}, \mathbf{X_{vb}}\} = \text{Downsampling}(\mathbf{X}'), \tag{10}$$

$$\{\mathbf{Y}_{\mathbf{hb}}', \mathbf{Y}_{\mathbf{vf}}', \mathbf{Y}_{\mathbf{vb}}'\} \to \{\mathbf{S}^{3}\mathbf{M}(\mathbf{X}_{\mathbf{hb}}), \mathbf{S}^{3}\mathbf{M}(\mathbf{X}_{\mathbf{vf}}), \mathbf{S}^{3}\mathbf{M}(\mathbf{X}_{\mathbf{vb}})\},\tag{11}$$

then followed by upsampling by a factor of 2 to restore the original feature scale, yielding \mathbf{Y}_{hb} , \mathbf{Y}_{vf} , and \mathbf{Y}_{vb} . Finally, the outputs from all four directions are summed to produce the final output \mathbf{Y} :

$$Y = Y_{hf} + Y_{hb} + Y_{vf} + Y_{vb}. \tag{12}$$

After getting the Mamba's output, a learnable channel-wise scaling factor γ_1 preserves critical spatial details during residual fusion:

$$\mathbf{Z} = \gamma_1 \odot \mathbf{X} + \mathbf{Y}. \tag{13}$$

Local texture refinement is then achieved through MLP-enhanced feature modulation:

$$\hat{\mathbf{Z}} = \gamma_2 \odot \mathbf{Z} + \text{MLP}(\text{LayerNorm}(\mathbf{Z})), \tag{14}$$

where γ_2 further recalibrates channel importance. Finally, **Z** passes through an MLP layer equipped with weighted residual connections to produce the output $\mathbf{Z} \in \mathbb{R}^{\hat{H} \times W \times C}$ of EMVM, enhancing feature extraction and representation capabilities.

3.2.3 Multi-scale Window Self-attention

Furthermore, we designed a multi-scale window self-attention module (MWSA), as shown in Fig. 3 (b) and Fig. 4, which dynamically refines local feature representations across hierarchical receptive fields to complement the global dependency modeling of EMVM. Designed to address the dual demands of high-frequency detail preservation and computational efficiency, MWSA processes an input feature map $\mathbf{X} \in \mathbb{R}^{H \times W \times C}$ through window-based self-attention

with progressively expanding window sizes. For a target window size w_s , the input is partitioned into $w_s \times w_s$ windows $\{\mathbf{W}_{i,j}\}$, each transformed via layer normalization and self-attention:

$$\mathbf{W}'_{i,j} = \text{LayerNorm}(\mathbf{W}_{i,j}),\tag{15}$$

$$Attn(\mathbf{Q}, \mathbf{K}, \mathbf{V}) = Softmax\left(\frac{\mathbf{Q}\mathbf{K}^{T}}{\sqrt{d_k}}\right)\mathbf{V},$$
(16)

where $\mathbf{Q} = \mathbf{W}'_{i,j}\mathbf{W}_Q$, $\mathbf{K} = \mathbf{W}'_{i,j}\mathbf{W}_K$, $\mathbf{V} = \mathbf{W}'_{i,j}\mathbf{W}_V$ are linear projections. The attended features are reconstructed into the spatial domain and fused with the original input through residual connections:

$$\mathbf{X}_{\text{attn}} = \text{WindowMerge}(\{\mathbf{W}'_{i,j}\}), \quad \mathbf{X}' = \mathbf{X} + \mathbf{X}_{\text{attn}}, \tag{17}$$

followed by an MLP for nonlinear refinement:

$$\mathbf{X}_{\text{out}} = \mathbf{X}' + \text{MLP}(\text{LayerNorm}(\mathbf{X}')). \tag{18}$$

By incrementally expanding window sizes from 8×8 to larger scales (+8 per module), MWSA hierarchically aggregates local-to-semiglobal contexts—small windows enhance details, while larger windows capture structural coherence. The design reduces global attention complexity, enabling efficient interaction between EMVM and MWSA. Their alternating use ensures integration of global recovery and multi-scale detail reconstruction, crucial for precise and efficient IR tasks.

3.3 Optimization Objective

For the super-resolution, we adopted single-scale L1 loss function to ensure fair comparison with existing studies [13]:

$$\mathcal{L}_{SR} = \|I_{HR} - \hat{I}_{HR}\|_1,\tag{19}$$

where $I_{\rm HR}$ and $\hat{I}_{\rm HR}$ denote high-resolution ground truth and reconstructed high-resolution image respectively. This single-scale formulation aligns with conventional evaluation protocols. For other tasks, we implemented deep supervision with multi-scale outputs. The composite loss integrates spatial and frequency domain constraints across scales:

$$\mathcal{L}_{\text{total}} = \sum_{i=1}^{3} \frac{1}{N_i} (\|P_i - I_i\|_1 + \lambda \|\mathcal{F}(P_i) - \mathcal{F}(I_i)\|_1),$$
 (20)

where P_i and I_i represent the predicted and target images at scale i, N_i is pixel count, and $\mathcal{F}(\cdot)$ denotes Fourier transform. The $\lambda=0.1$ balance factor follows established practices [10]. This multi-scale dual-domain design enhances feature learning for improved restoration quality.

4 Experiments and Analysis

4.1 Datasets and Experimental Settings

To comprehensively assess RestorMixer across diverse degradation scenarios, we conduct evaluations on both single and composite image restoration tasks. The single degradation tasks include deraining, desnowing and super-resolution. For deraining, we use Rain100L [25] (light rain), Rain100H [25] (heavy rain), Test1200 [26] (dense mild rain), and Test2800 [27] (multi-directional rain). For desnowing, we evaluate on the CSD [28] dataset. Super-resolution models are trained on DIV2K [29] with upscaling factors of $\times 2$, $\times 3$, and $\times 4$, and tested on Set5 [30], Set14 [31], BSDS100 [32], Urban100 [33], and Manga109 [34]. Composite degradation is trained and evaluated on the CDD-11 [16] benchmark, which includes 4 single degradations (Low, Haze, Rain, Snow), 4 dual-combinations (Low + Haze, Low + Rain, Low + Snow, Haze + Rain), and 3 triple-combinations (Low+Haze+Rain, Haze+Snow).

RestorMixer adopts a unified 3-stage encoder-decoder architecture with 4 basic blocks per stage for most tasks. For super-resolution, Adjustments of the model are in the *Supplementary Material*. All models are trained using the Adam [35] optimizer, and data augmentation includes random cropping and horizontal flipping. The learning rate follows a cosine annealing schedule with task-specific initialization. Following common practice, PSNR and SSIM are used for evaluation. Following the previous works, deraining results are reported in YCbCr and all others in RGB. All experiments are run on NVIDIA RTX 4090 GPUs.

M-41 1-	Rain100H		Rain100L		Test2800		Test1200		Average		Params	Flops
Methods	S PSNR		PSNR	SSIM	PSNR	SSIM	PSNR	SSIM	PSNR	SSIM	(M)	(G)
MSPFN [36]	28.66	0.860	32.40	0.933	32.82	0.930	32.39	0.916	31.57	0.910	13.22	604.70
MPRNet [19]	30.41	0.890	36.40	0.965	33.64	0.938	32.91	0.916	33.34	0.927	3.64	141.28
MAXIM [37]	30.81	0.904	38.06	0.977	33.80	0.943	32.37	0.922	33.76	0.937	6.10	93.60
Restormer [11]	31.46	0.904	38.99	0.978	34.18	0.944	33.19	0.926	34.46	0.938	26.10	140.99
IDT [5]	29.95	0.898	37.01	0.971	33.38	0.929	31.38	0.913	32.93	0.928	16.00	61.90
IRNext [10]	31.64	0.902	38.24	0.972	-	-	-	-	-	-	13.21	114.00
IR-SDE [38]	31.65	0.904	38.30	0.980	30.42	0.891	-	-	-	-	135.30	119.10
DRSformer [39]	31.66	0.901	<u>39.23</u>	0.979	34.19	0.943	33.34	0.926	34.61	0.937	33.70	60.74
MFDNet [40]	30.48	0.899	37.61	0.973	33.55	0.939	33.01	0.925	33.66	0.934	4.74	68.71
MambaIR [15]	30.62	0.893	38.78	0.977	33.58	0.927	32.56	0.923	33.89	0.930	31.51	80.64
VMambaIR [14]	31.66	0.909	39.09	0.979	34.01	0.944	33.33	0.926	34.52	0.940	-	-
FreqMamba [4]	<u>31.74</u>	0.912	39.18	0.981	<u>34.25</u>	0.951	<u>33.36</u>	0.931	34.63	0.944	14.52	36.49
Ours	33.03	0.930	39.53	0.984	34.37	0.944	34.93	0.938	35.47	0.949	2.80	25.16

Table 1: Quantitative comparison of various methods on rain streak removal on four public rain datasets.

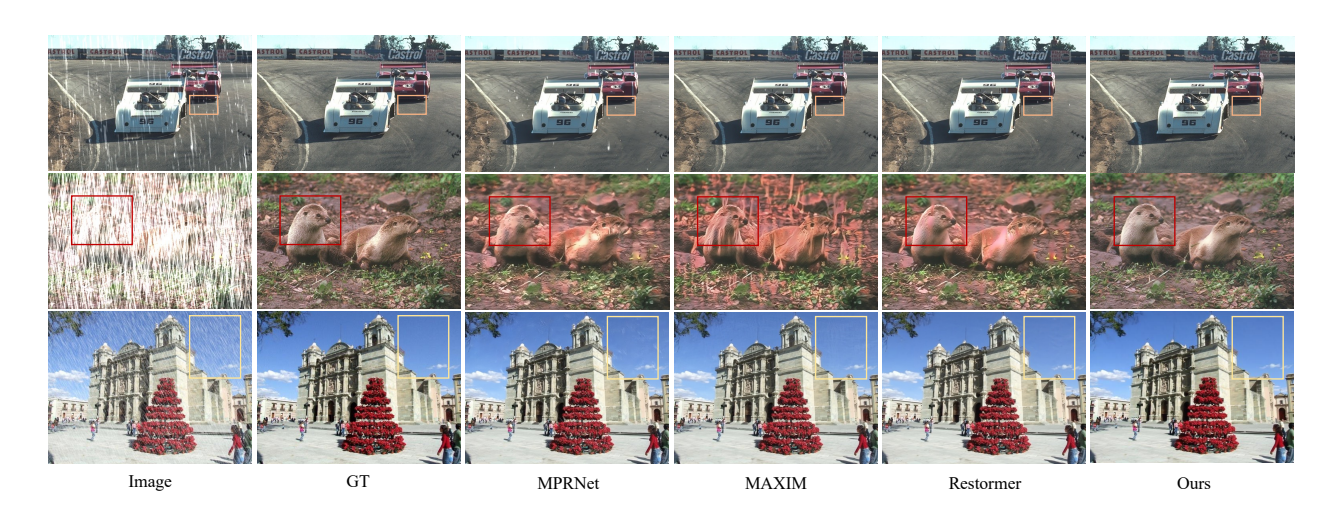


Figure 5: Visual comparison with SOTA methods under various rain intensities.

4.2 Rainy Streak Removal of Single Image

RestorMixer achieves state-of-the-art performance on four deraining benchmarks: Rain100H [25], Rain100L [25], Test2800 [27], and Test1200 [26]. As shown in Tab. 1, it obtains an average PSNR of 35.47 dB and SSIM of 0.949, clearly outperforming existing methods. The visual results in Fig. 5 confirm its advantage in restoring details and removing rain streaks.

On the challenging Test1200 dataset, RestorMixer achieves a PSNR of 34.93 dB, surpassing the second-best method by 1.57 dB. In heavy rain scenarios such as Rain100H, the improvement reaches 1.29 dB, highlighting its strong capacity to model global and local features, as well as its generalization of diverse rain patterns. Despite its strong performance, RestorMixer maintains a lightweight design with only 2.80M parameters and 25.16G FLOPs, the lowest among all compared methods, demonstrating an excellent trade-off between accuracy and efficiency, and strong potential for deployment in real-world, resource-constrained environments.

4.3 Single Image Super Resolution

In the single-image super-resolution, we evaluate the performance of RestorMixer under lightweight settings with upscaling factors of $2\times, 3\times$, and $4\times$. All models are trained on the DIV2K [29] dataset and evaluated on five widely-used

Table 2: Super-resolution performance comparison on benchmark datasets.

Nr. 41 - 1	G 1	//D	MAG	S	et5	Se	t14	BSD	S100	Urba	an100	Man	ga109
Methods	Scale	#Param	MACS	PSNR	SSIM								
CARN [42]	$\times 2$		222.8G										
IMDN [43]	$\times 2$	694K	158.8G	38.00	0.9605	33.63	0.9177	32.19	0.8996	32.17	0.9283	38.88	0.9774
LAPAR-A [44]	$\times 2$	548K	171.0G	38.01	0.9605	33.62	0.9183	32.19	0.8999	32.10	0.9283	38.67	0.9772
LatticeNet [45]	$\times 2$	756K	169.5G	38.15	0.9610	33.78	0.9193	32.25	0.9005	32.43	0.9302	-	-
SwinIR-light [12]	$\times 2$	910K	122.2G	38.14	0.9611	33.86	0.9206	32.31	0.9012	32.76	0.9340	39.12	0.9783
SRFormer-light [41]	$\times 2$	853K	236G	<u>38.23</u>	0.9613	33.94	0.9209	32.36	0.9019	<u>32.91</u>	0.9353	<u>39.28</u>	0.9785
MambaIR [15]	$\times 2$	905K	167.1G	38.13	0.9610	<u>33.95</u>	0.9208	32.31	0.9013	32.85	0.9349	39.20	0.9782
Ours	$\times 2$	1066K	93.7G	38.22	0.9614	33.96	0.9217	32.33	0.9017	32.94	0.9358	39.33	0.9782
CARN [42]	$\times 3$	1,592K	118.8G	34.29	0.9255	30.29	0.8407	29.06	0.8034	28.06	0.8493	33.50	0.9440
IMDN [43]	$\times 3$	703K	71.5G	34.36	0.9270	30.32	0.8417	29.09	0.8046	28.17	0.8519	33.61	0.9445
LAPAR-A [44]	$\times 3$	544K	114.0G	34.36	0.9267	30.34	0.8421	29.11	0.8054	28.15	0.8523	33.51	0.9441
LatticeNet [45]	$\times 3$	765K	76.3G	34.53	0.9281	30.39	0.8424	29.15	0.8059	28.33	0.8538	-	-
SwinIR-light [12]	$\times 3$	918K	55.4G	34.62	0.9289	30.54	0.8463	29.20	0.8082	28.66	0.8624	33.98	0.9478
SRFormer-light [41]	$\times 3$	861K	105G	34.67	0.9296	30.57	0.8469	29.26	0.8099	28.81	0.8655	<u>34.19</u>	0.9489
MambaIR [15]	$\times 3$	913K	74.5G	34.63	0.9288	30.54	0.8459	29.23	0.8084	28.70	0.8631	34.12	0.9479
Ours	$\times 3$	1074K	43.0G	34.70	0.9298	30.65	0.8476	29.28	0.8099	28.81	0.8654	34.37	0.9492
CARN [42]	$\times 4$	1,592K	90.9G	32.13	0.8937	28.60	0.7806	27.58	0.7349	26.07	0.7837	30.47	0.9084
IMDN [43]	$\times 4$	715K	40.9G	32.21	0.8948	28.58	0.7811	27.56	0.7353	26.04	0.7838	30.45	0.9075
LAPAR-A [44]	$\times 4$	659K	94.0G	32.15	0.8944	28.61	0.7818	27.61	0.7366	26.14	0.7871	30.42	0.9074
LatticeNet [45]	$\times 4$	777K	43.6G	32.30	0.8962	28.68	0.7830	27.62	0.7367	26.25	0.7873	-	-
SwinIR-light [12]	$\times 4$	930K	31.8G	32.44	0.8976	28.77	0.7858	27.69	0.7406	26.47	0.7980	30.92	0.9151
SRFormer-light [41]	$\times 4$	873K	62.8G	<u>32.51</u>	0.8988	28.82	0.7872	27.73	0.7422	26.67	0.8032	31.17	0.9165
MambaIR [15]	$\times 4$	924K	42.3G	32.42	0.8977	28.74	0.7847	27.68	0.7400	26.52	0.7983	30.94	0.9135
Ours	$\times 4$	1085K	23.9G	32.54	0.8992	28.85	0.7876	<u>27.72</u>	0.7422	<u>26.60</u>	0.8013	31.17	<u>0.9163</u>



Figure 6: Visual comparison with general and specialized super-resolution methods under lightweight settings.

benchmarks with diverse content ranging from simple patterns to complex textures. As shown in Tab. 2, RestorMixer achieves competitive performance compared with both general and specialized SR methods. Although some SR expert methods, such as SRFormer-light [41] achieve the best results on individual benchmarks, our method strikes a better balance between performance and efficiency. Visual comparisons in Fig. 6 further support this observation: our method effectively restores high-frequency textures and details, producing clean and natural results even in challenging regions.

4.4 Single Image De-snowing

In the single image desnowing task, we evaluated the performance of RestorMixer on the CSD (2000) [28] dataset. The experimental results are shown in Tab. 3, where RestorMixer achieves the best restoration results in terms of PSNR and SSIM, reaching 39.88dB and 0.99, significantly outperforming other methods.

Table 3: Performance comparison of different methods on the CSD for snow removal.

Methods	PSNR	SSIM	Params(M)	FLOPs(G)
DesnowNet [46]	20.13	0.81	15.6	1.7K
HDCW-Net [47]	29.06	0.91	6.99	9.78
SMGARN [48]	31.93	0.95	6.86	450.30
TransWeather [49]	31.76	0.93	21.90	5.64
MPRNet [19]	33.98	0.97	3.64	141.28
DGUNet [50]	34.74	0.97	12.18	199.74
Uformer [18]	33.80	0.96	9.03	19.82
Restormer [11]	35.43	0.97	26.10	140.99
NAFNet [51]	35.13	0.97	22.40	12.12
SnowFormer [7]	<u>39.45</u>	0.98	8.38	19.44
MB-TaylorFormer [52]	37.10	0.98	2.68	38.5
Ours	39.88	0.99	2.80	25.16

4.5 Mixed Degradation Image Restoration

We evaluate RestorMixer on the CDD-11 [16] dataset for mixed degradation restoration. All models are trained on the full 11-subset training set using a unified strategy, without per-task tuning. Competing methods are categorized into one-to-one, one-to-many, and one-to-composite according to their adaptation mechanisms. As shown in Tab. 4, RestorMixer achieves strong performance using a simple and general architecture without task-specific designs, scheduling strategies, or adaptive modules. It outperforms all one-to-one and one-to-many models, and performs on par with OneRestore [16] — despite the latter being tailored for composite degradations. Notably, RestorMixer achieves the highest SSIM of 0.8807, indicating superior structural fidelity. With fewer parameters and competitive results, RestorMixer offers a better trade-off between performance and efficiency. The visual results in Fig. 7 further confirm its effectiveness in handling complex degradations.

5 Ablation Study

To evaluate the effectiveness of each design in RestorMixer, we perform ablation studies on Rain100L [25] and Rain100H [25] under identical training settings. Evaluation metrics include PSNR and SSIM for restoration quality, FLOPs (G) and Params (M) for complexity, and inference speed (ms) and memory usage for practical efficiency. The baseline model adopts a 3-level encoder-decoder architecture, with 4 hybrid blocks per layer and multi-scale attention windows of 8×8 and 16×16 . Inference speed is measured as the average over $100\ 256\times 256$ patches, and memory refers to peak GPU usage during inference.

5.1 Impact of Block Depth

We investigate the effect of the number of stacked hybrid blocks in each encoder/decoder stage, comparing 2, 4 (baseline), and 6 blocks. Results in Table 5 show that increasing from 2 to 4 blocks improves both PSNR and SSIM, particularly on Rain100H with more complex rain streaks, highlighting the benefit of deeper architectures for multi-scale learning. However, increasing to 6 blocks provides little improvement while significantly increasing computational cost, memory usage, and latency. Therefore, 4 blocks strike the best balance between performance and efficiency.

5.2 Effect of Multi-Scale Window Attention

We evaluate the effectiveness of Multi-scale Window Self-attention (MWSA) by comparing the default multi-scale configuration ($8 \times 8 \to 16 \times 16$) with two fixed-size alternatives: all 8×8 and all 16×16 . Results in Table 6 show

Table 4: Performance	comparison of different	t methods on mixed	degradation image restoration.
Table 4. I citorinance	comparison of uniteren	i memous on macu	degradation image restoration.

	Methods	PSNR	SSIM	Params(M)	
	MIRNet [53]	25.97	0.8474	31.79	
	MPRNet [19]	25.47	0.8555	15.74	
	Restormer [11]	26.99	0.8646	26.99	
One-to-One	DGUNet [50]	26.92	0.8559	17.33	
One-to-One	NAFNet [51]	24.13	0.7964	24.13	
	SRUDC [54]	27.64	0.8600	6.80	
	OKNet [55]	26.33	0.8605	4.72	
	AirNet [56]	23.75	0.8140	8.93	
	TransWeather [49]	23.13	0.7810	21.90	
One-to-Many	WeatherDiff [57]	22.49	0.7985	82.96	
	PromptIR [58]	25.90	0.8499	38.45	
	WGWSNet [59]	26.96	0.8626	25.76	
One-to-Composite	OneRestore [16]	28.47	0.8784	5.98	
One-to-One	Ours	28.01	0.8807	2.80	
		GT	Restormer	OKNet	
Low (No	aise)		Restormer		
Low (No	ise)	GT PromptIR GT		OKNet OKNet	

Figure 7: Visual comparison under low-light and composite degradations (Low+Haze+Rain).

significant performance drops with fixed window sizes, especially on Rain100H. This demonstrates that fixed receptive fields fail to adapt to spatial variations, limiting the capture of both local textures and global semantics. In contrast, the hierarchical window setting allows more flexible context aggregation, improving robustness to diverse rain patterns.

5.3 Component-Level Structure Ablation

We investigate the role of key components through four controlled experiments, each modifying or removing a specific part of the baseline model. Results are shown in Table 7.

The "NoDSM" variant removes downsampling in EMVM, keeping all operations at full resolution. While it retains detailed spatial information, it suffers from high computational cost and redundancy, demonstrating that long-range modeling is more efficient at lower resolutions. In the "NoRDCNN" variant, we replace the high-resolution RDCNN

Table 5: Ablation on number of blocks per stage.

#Blocks	Rain PSNR	100L SSIM	Rain: PSNR	100H SSIM	FLOPs (G)	Params (M)	Speed (ms)	Memory (G)
2						16.92		
4	39.53	0.984	33.03	0.930	2.80	25.16	20.55	2.22
6	39.58	0.985	32.86	0.929	3.85	34.32	29.87	3.82

Table 6: Ablation on window size setting in MWSA.

#Window	Rain	Rain100L		Rain100H		Params	Speed	Memory
Size	PSNR	SSIM	PSNR	SSIM	(G)	(M)	(ms)	(G)
$(8 \rightarrow 16)$	39.53	0.984	33.03	0.930	2.80	25.16	20.55	2.22
8×8	39.29	0.984	32.14	0.920	2.80	25.05	20.53	2.05
16×16	39.08	0.984	32.05	0.919	2.80	25.26	20.63	2.35

Table 7: Ablation on structural components of RestorMixer.

#Variant	Rain PSNR		Rain PSNR		FLOPs (G)	Params (M)	Speed (ms)	Memory (G)
Baseline	3 9.53	0.984	33.03	0.930	2.80	25.16	20.55	2.22
NoDSM	39.32	0.984	32.62	0.925	2.76	27.56	25.66	2.78
NoRDCNN	39.44	0.984	32.66	0.927	2.83	25.89	31.51	5.28
NoMWSA	38.91	0.983	30.28	0.902	2.86	25.41	18.17	1.81
FullTA	38.82	0.983	32.30	0.921	2.80	24.98	28.52	2.04

with the same M-T blocks. This introduces architectural uniformity but slightly degrades fine detail restoration, highlighting the importance of local convolutional priors in early decoding stages. The "NoMWSA" variant removes MWSA, replacing it with pure RDCNN in hybrid blocks. Performance, especially on Rain100H, drops significantly, showing that MWSA is crucial for capturing dynamic spatial structures. Unlike static CNN kernels, window attention adapts to the input, improving model flexibility. The "FullTA" variant replaces window self-attention with the transposed attention module from Restormer [11]. Although it enables global modeling at channel dimension, it lacks spatial selectivity compared to MWSA and incurs higher computational cost, resulting in a poorer efficiency-performance trade-off.

6 Conclusion

In this paper, we address the limitation in performance improvement of current models for various IR tasks, which are typically designed based on a single underlying architecture. We propose a novel IR model named RestorMixer, which is meticulously constructed by integrating three heterogeneous underlying architectures. Specifically, RestorMixer capitalizes on the individual strengths of these three structures: it employs RDCNN block for its efficient parallel computation and ability to extract shallow features, to process the highest-resolution feature maps in the model's encoding/decoding stages; it utilizes EMVM block to rapidly model global feature dependencies, and optimizes the computational redundancy and memory attenuation issues present in the classical multi-directional SSM scanning mechanism; and it further refines local feature extraction and representation using multi-scale window self-attention. Extensive experimental validation demonstrates that the proposed RestorMixer achieves leading performance on multiple image degradation restoration benchmark datasets, including single degradation and composite degradation IR, while also exhibiting highly efficient inference speed.

References

- [1] Mengyin Liu, Chao Zhu, Shiqi Ren, and Xu-Cheng Yin. Unsupervised multi-view pedestrian detection. In *Proceedings of the 32nd ACM International Conference on Multimedia*, pages 1034–1042, 2024.
- [2] Zhiwen Wang, Yuhui Wu, Zheng Wang, Jiwei Wei, Tianyu Li, Guoqing Wang, Yang Yang, and Hengtao Shen. Cascaded adversarial attack: Simultaneously fooling rain removal and semantic segmentation networks. In *Proceedings of the 32nd ACM International Conference on Multimedia*, pages 2136–2145, 2024.
- [3] Jingfan Tan, Hyunhee Park, Ying Zhang, Tao Wang, Kaihao Zhang, Xiangyu Kong, Pengwen Dai, Zikun Liu, and Wenhan Luo. Blind face video restoration with temporal consistent generative prior and degradation-aware prompt. In *Proceedings of the 32nd ACM International Conference on Multimedia*, pages 1417–1426, 2024.
- [4] Zhen Zou, Hu Yu, Jie Huang, and Feng Zhao. Freqmamba: Viewing mamba from a frequency perspective for image deraining. In *Proceedings of the 32nd ACM International Conference on Multimedia*, pages 1905–1914, 2024.
- [5] Jie Xiao, Xueyang Fu, Aiping Liu, Feng Wu, and Zheng-Jun Zha. Image de-raining transformer. *IEEE transactions on pattern analysis and machine intelligence*, 45(11):12978–12995, 2022.
- [6] Ting Zhang, Nanfeng Jiang, Hongxin Wu, Keke Zhang, Yuzhen Niu, and Tiesong Zhao. Hcsd-net: Single image desnowing with color space transformation. In *Proceedings of the 31st ACM International Conference on Multimedia*, pages 8125–8133, 2023.
- [7] Sixiang Chen, Tian Ye, Yun Liu, and Erkang Chen. Snowformer: Context interaction transformer with scale-awareness for single image desnowing. *arXiv* preprint arXiv:2208.09703, 2022.
- [8] Wengyi Zhan, Mingbao Lin, Chia-Wen Lin, and Rongrong Ji. Anysr: Realizing image super-resolution as any-scale, any-resource. *IEEE Transactions on Image Processing*, 2024.
- [9] Chao Dong, Chen Change Loy, Kaiming He, and Xiaoou Tang. Image super-resolution using deep convolutional networks. *IEEE transactions on pattern analysis and machine intelligence*, 38(2):295–307, 2015.
- [10] Yuning Cui, Wenqi Ren, Sining Yang, Xiaochun Cao, and Alois Knoll. Irnext: Rethinking convolutional network design for image restoration. In *International conference on machine learning*, 2023.
- [11] Syed Waqas Zamir, Aditya Arora, Salman Khan, Munawar Hayat, Fahad Shahbaz Khan, and Ming-Hsuan Yang. Restormer: Efficient transformer for high-resolution image restoration. In *Proceedings of the IEEE/CVF conference on computer vision and pattern recognition*, pages 5728–5739, 2022.
- [12] Jingyun Liang, Jiezhang Cao, Guolei Sun, Kai Zhang, Luc Van Gool, and Radu Timofte. Swinir: Image restoration using swin transformer. In *Proceedings of the IEEE/CVF international conference on computer vision*, pages 1833–1844, 2021.
- [13] Albert Gu and Tri Dao. Mamba: Linear-time sequence modeling with selective state spaces. *arXiv preprint arXiv:2312.00752*, 2023.
- [14] Yuan Shi, Bin Xia, Xiaoyu Jin, Xing Wang, Tianyu Zhao, Xin Xia, Xuefeng Xiao, and Wenming Yang. Vmambair: Visual state space model for image restoration. *IEEE Transactions on Circuits and Systems for Video Technology*, 2025.
- [15] Hang Guo, Jinmin Li, Tao Dai, Zhihao Ouyang, Xudong Ren, and Shu-Tao Xia. Mambair: A simple baseline for image restoration with state-space model. In *European conference on computer vision*, pages 222–241. Springer, 2024.
- [16] Yu Guo, Yuan Gao, Yuxu Lu, Huilin Zhu, Ryan Wen Liu, and Shengfeng He. Onerestore: A universal restoration framework for composite degradation. In *European Conference on Computer Vision*, pages 255–272. Springer, 2024.
- [17] Cong Wang, Liyan Wang, Jie Mu, Chengjin Yu, and Wei Wang. Progressive local and non-local interactive networks with deeply discriminative training for image deraining. In *Proceedings of the 32nd ACM International Conference on Multimedia*, pages 10326–10335, 2024.
- [18] Zhendong Wang, Xiaodong Cun, Jianmin Bao, Wengang Zhou, Jianzhuang Liu, and Houqiang Li. Uformer: A general u-shaped transformer for image restoration. In *Proceedings of the IEEE/CVF conference on computer vision and pattern recognition*, pages 17683–17693, 2022.
- [19] Syed Waqas Zamir, Aditya Arora, Salman Khan, Munawar Hayat, Fahad Shahbaz Khan, Ming-Hsuan Yang, and Ling Shao. Multi-stage progressive image restoration. In *Proceedings of the IEEE/CVF conference on computer vision and pattern recognition*, pages 14821–14831, 2021.

- [20] Ali Hatamizadeh and Jan Kautz. Mambavision: A hybrid mamba-transformer vision backbone. arXiv preprint arXiv:2407.08083, 2024.
- [21] Jun Ma, Feifei Li, and Bo Wang. U-mamba: Enhancing long-range dependency for biomedical image segmentation. *arXiv preprint arXiv:2401.04722*, 2024.
- [22] Yuheng Shi, Minjing Dong, and Chang Xu. Multi-scale vmamba: Hierarchy in hierarchy visual state space model. arXiv preprint arXiv:2405.14174, 2024.
- [23] Dongchen Han, Ziyi Wang, Zhuofan Xia, Yizeng Han, Yifan Pu, Chunjiang Ge, Jun Song, Shiji Song, Bo Zheng, and Gao Huang. Demystify mamba in vision: A linear attention perspective. *arXiv preprint arXiv:2405.16605*, 2024.
- [24] Yue Liu, Yunjie Tian, Yuzhong Zhao, Hongtian Yu, Lingxi Xie, Yaowei Wang, Qixiang Ye, Jianbin Jiao, and Yunfan Liu. Vmamba: Visual state space model. *Advances in neural information processing systems*, 37:103031–103063, 2024.
- [25] Wenhan Yang, Robby T Tan, Jiashi Feng, Jiaying Liu, Zongming Guo, and Shuicheng Yan. Deep joint rain detection and removal from a single image. In *Proceedings of the IEEE conference on computer vision and pattern recognition*, pages 1357–1366, 2017.
- [26] He Zhang and Vishal M Patel. Density-aware single image de-raining using a multi-stream dense network. In *Proceedings of the IEEE conference on computer vision and pattern recognition*, pages 695–704, 2018.
- [27] Xueyang Fu, Jiabin Huang, Delu Zeng, Yue Huang, Xinghao Ding, and John Paisley. Removing rain from single images via a deep detail network. In *Proceedings of the IEEE conference on computer vision and pattern recognition*, pages 3855–3863, 2017.
- [28] Wei-Ting Chen, Hao-Yu Fang, Cheng-Lin Hsieh, Cheng-Che Tsai, I Chen, Jian-Jiun Ding, Sy-Yen Kuo, et al. All snow removed: Single image desnowing algorithm using hierarchical dual-tree complex wavelet representation and contradict channel loss. In *Proceedings of the IEEE/CVF international conference on computer vision*, pages 4196–4205, 2021.
- [29] Radu Timofte, Eirikur Agustsson, Luc Van Gool, Ming-Hsuan Yang, and Lei Zhang. Ntire 2017 challenge on single image super-resolution: Methods and results. In *Proceedings of the IEEE conference on computer vision and pattern recognition workshops*, pages 114–125, 2017.
- [30] Marco Bevilacqua, Aline Roumy, Christine Guillemot, and Marie Line Alberi-Morel. Low-complexity single-image super-resolution based on nonnegative neighbor embedding. 2012.
- [31] Roman Zeyde, Michael Elad, and Matan Protter. On single image scale-up using sparse-representations. In *Curves and Surfaces: 7th International Conference, Avignon, France, June 24-30, 2010, Revised Selected Papers 7*, pages 711–730. Springer, 2012.
- [32] David Martin, Charless Fowlkes, Doron Tal, and Jitendra Malik. A database of human segmented natural images and its application to evaluating segmentation algorithms and measuring ecological statistics. In *Proceedings eighth IEEE international conference on computer vision. ICCV 2001*, volume 2, pages 416–423. IEEE, 2001.
- [33] Jia-Bin Huang, Abhishek Singh, and Narendra Ahuja. Single image super-resolution from transformed self-exemplars. In *Proceedings of the IEEE conference on computer vision and pattern recognition*, pages 5197–5206, 2015
- [34] Yusuke Matsui, Kota Ito, Yuji Aramaki, Azuma Fujimoto, Toru Ogawa, Toshihiko Yamasaki, and Kiyoharu Aizawa. Sketch-based manga retrieval using manga109 dataset. *Multimedia tools and applications*, 76:21811–21838, 2017
- [35] Diederik P Kingma and Jimmy Ba. Adam: A method for stochastic optimization. arXiv preprint arXiv:1412.6980, 2014.
- [36] Kui Jiang, Zhongyuan Wang, Peng Yi, Chen Chen, Baojin Huang, Yimin Luo, Jiayi Ma, and Junjun Jiang. Multi-scale progressive fusion network for single image deraining. In *Proceedings of the IEEE/CVF conference on computer vision and pattern recognition*, pages 8346–8355, 2020.
- [37] Zhengzhong Tu, Hossein Talebi, Han Zhang, Feng Yang, Peyman Milanfar, Alan Bovik, and Yinxiao Li. Maxim: Multi-axis mlp for image processing. In *Proceedings of the IEEE/CVF conference on computer vision and pattern recognition*, pages 5769–5780, 2022.
- [38] Ziwei Luo, Fredrik K Gustafsson, Zheng Zhao, and Jens Sjölund. Image restoration with mean-reverting stochastic differential equations. In *International Conference on Machine Learning (ICML), Honolulu, Hawaii, USA, 23-29 July, 2023*, volume 202, pages 23045–23066, 2023.

- [39] Xiang Chen, Hao Li, Mingqiang Li, and Jinshan Pan. Learning a sparse transformer network for effective image deraining. In *Proceedings of the IEEE/CVF conference on computer vision and pattern recognition*, pages 5896–5905, 2023.
- [40] Qiong Wang, Kui Jiang, Zheng Wang, Wenqi Ren, Jianhui Zhang, and Chia-Wen Lin. Multi-scale fusion and decomposition network for single image deraining. *IEEE Transactions on Image Processing*, 33:191–204, 2023.
- [41] Yupeng Zhou, Zhen Li, Chun-Le Guo, Song Bai, Ming-Ming Cheng, and Qibin Hou. Srformer: Permuted self-attention for single image super-resolution. In *Proceedings of the IEEE/CVF International Conference on Computer Vision*, pages 12780–12791, 2023.
- [42] Namhyuk Ahn, Byungkon Kang, and Kyung-Ah Sohn. Fast, accurate, and lightweight super-resolution with cascading residual network. In *Proceedings of the European conference on computer vision (ECCV)*, pages 252–268, 2018.
- [43] Zheng Hui, Xinbo Gao, Yunchu Yang, and Xiumei Wang. Lightweight image super-resolution with information multi-distillation network. In *Proceedings of the 27th acm international conference on multimedia*, pages 2024–2032, 2019.
- [44] Wenbo Li, Kun Zhou, Lu Qi, Nianjuan Jiang, Jiangbo Lu, and Jiaya Jia. Lapar: Linearly-assembled pixel-adaptive regression network for single image super-resolution and beyond. *Advances in Neural Information Processing Systems*, 33:20343–20355, 2020.
- [45] Wenjie Luo, Yujia Li, Raquel Urtasun, and Richard Zemel. Understanding the effective receptive field in deep convolutional neural networks. *Advances in neural information processing systems*, 29, 2016.
- [46] Yun-Fu Liu, Da-Wei Jaw, Shih-Chia Huang, and Jenq-Neng Hwang. Desnownet: Context-aware deep network for snow removal. *IEEE Transactions on Image Processing*, 27(6):3064–3073, 2018.
- [47] Wei-Ting Chen, Hao-Yu Fang, Cheng-Lin Hsieh, Cheng-Che Tsai, I Chen, Jian-Jiun Ding, Sy-Yen Kuo, et al. All snow removed: Single image desnowing algorithm using hierarchical dual-tree complex wavelet representation and contradict channel loss. In *Proceedings of the IEEE/CVF international conference on computer vision*, pages 4196–4205, 2021.
- [48] Bodong Cheng, Juncheng Li, Ying Chen, and Tieyong Zeng. Snow mask guided adaptive residual network for image snow removal. *Computer Vision and Image Understanding*, 236:103819, 2023.
- [49] Jeya Maria Jose Valanarasu, Rajeev Yasarla, and Vishal M Patel. Transweather: Transformer-based restoration of images degraded by adverse weather conditions. In *Proceedings of the IEEE/CVF conference on computer vision and pattern recognition*, pages 2353–2363, 2022.
- [50] Chong Mou, Qian Wang, and Jian Zhang. Deep generalized unfolding networks for image restoration. In *Proceedings of the IEEE/CVF conference on computer vision and pattern recognition*, pages 17399–17410, 2022.
- [51] Liangyu Chen, Xiaojie Chu, Xiangyu Zhang, and Jian Sun. Simple baselines for image restoration. In *European conference on computer vision*, pages 17–33. Springer, 2022.
- [52] Yuwei Qiu, Kaihao Zhang, Chenxi Wang, Wenhan Luo, Hongdong Li, and Zhi Jin. Mb-taylorformer: Multibranch efficient transformer expanded by taylor formula for image dehazing. In *Proceedings of the IEEE/CVF International Conference on Computer Vision*, pages 12802–12813, 2023.
- [53] Syed Waqas Zamir, Aditya Arora, Salman Khan, Munawar Hayat, Fahad Shahbaz Khan, Ming Hsuan Yang, and Ling Shao. Learning enriched features for real image restoration and enhancement. In 16th European Conference on Computer Vision, ECCV 2020, pages 492–511. Springer Science and Business Media Deutschland GmbH, 2020.
- [54] Binbin Song, Xiangyu Chen, Shuning Xu, and Jiantao Zhou. Under-display camera image restoration with scattering effect. In *Proceedings of the IEEE/CVF International Conference on Computer Vision*, pages 12580–12589, 2023.
- [55] Yuning Cui, Wenqi Ren, and Alois Knoll. Omni-kernel network for image restoration. In *Proceedings of the AAAI conference on artificial intelligence*, volume 38, pages 1426–1434, 2024.
- [56] Boyun Li, Xiao Liu, Peng Hu, Zhongqin Wu, Jiancheng Lv, and Xi Peng. All-in-one image restoration for unknown corruption. In *Proceedings of the IEEE/CVF conference on computer vision and pattern recognition*, pages 17452–17462, 2022.
- [57] Ozan Özdenizci and Robert Legenstein. Restoring vision in adverse weather conditions with patch-based denoising diffusion models. *IEEE Transactions on Pattern Analysis and Machine Intelligence*, 45(8):10346–10357, 2023.
- [58] Vaishnav Potlapalli, Syed Waqas Zamir, Salman H Khan, and Fahad Shahbaz Khan. Promptir: Prompting for all-in-one image restoration. *Advances in Neural Information Processing Systems*, 36:71275–71293, 2023.

[59] Yurui Zhu, Tianyu Wang, Xueyang Fu, Xuanyu Yang, Xin Guo, Jifeng Dai, Yu Qiao, and Xiaowei Hu. Learning weather-general and weather-specific features for image restoration under multiple adverse weather conditions. In *Proceedings of the IEEE/CVF conference on computer vision and pattern recognition*, pages 21747–21758, 2023.